Single-layer and bilayer graphene superlattices: collimation, additional Dirac points and Dirac lines

By Michaël Barbier, Panagiotis Vasilopoulos, and François M. Peeters

[1]*Department of Physics, University of Antwerp,*
Groenenborgerlaan 171, B-2020 Antwerpen, Belgium
[2]*Department of Physics, Concordia University,*
7141 Sherbrooke Ouest, Montréal, Quebec, Canada H4B 1R6

We review the energy spectrum and transport properties of several types of one-dimensional superlattices (SLs) on single-layer and bilayer graphene. In single-layer graphene, for certain SL parameters an electron beam incident on a SL is highly collimated. On the other hand there are extra Dirac points generated for other SL parameters. Using rectangular barriers allows us to find analytic expressions for the location of new Dirac points in the spectrum and for the renormalization of the electron velocities. The influence of these extra Dirac points on the conductivity is investigated. In the limit of δ-function barriers, the transmission T through, conductance G of a finite number of barriers as well as the energy spectra of SLs are *periodic* functions of the dimensionless strength P of the barriers, $P\delta(x) = V(x)/\hbar v_F$, with v_F the Fermi velocity. For a Kronig-Penney SL with alternating sign of the height of the barriers the Dirac point becomes a Dirac line for $P = \pi/2 + n\pi$ with n an integer. In bilayer graphene, with an appropriate bias applied to the barriers and wells, we show that several new types of SLs are produced and two of them are similar to type I and type II semiconductor SLs. Similar as in single-layer graphene extra "Dirac" points are found. Non-ballistic transport is also considered.

Keywords: graphene; electron transport; two-dimensional crystals

1. Introduction

Since the experimental realisation of graphene (Novoselov *et al.*, 2004) in 2004, this one-atom thick layer of carbon atoms has attracted the attention of the scientific world. This attraction pole was created by the prediction that the carriers in graphene behave as massless relativistic fermions moving in two dimensions. The latter particles, which are described by the Dirac-Weyl Hamiltonian, possess interesting properties such as a gapless and linear-in-wave vector electronic spectrum, a perfect transmission, at normal incidence, through any potential barrier, i.e., the Klein paradox (Klein, 1929; Katsnelson *et al.*, 2006; Pereira Jr *et al.*, 2010; Roslyak *et al.*, 2010), which was recently addressed experimentally (Young & Kim, 2009; Huard *et al.*, 2007), the zitterbewegung (Schliemann *et al.*, 2005; Winkler *et al.*, 2007; Zawadzki, 2005), etc., see Ref. (Castro Neto *et al.*, 2009) and (Abergel *et al.*, 2010) for recent reviews. On the other hand, in bilayer graphene the carriers exhibit

a very different but extraordinary electronic behaviour, such as being chiral (Mc-Cann, 2006; Katsnelson *et al.*, 2006) but with a different pseudospin (=1) than in single-layer graphene (=1/2). Although their spectrum is parabolic in wave vector and also gapless, it is possible to create an energy gap by applying a perpendicular electric field on a bilayer graphene sample (Castro *et al.*, 2007). This allows one to electrostatically create quantum dots in bilayer graphene (Pereira Jr *et al.*, 2007*b*) and enrich its technological capabilities.

In previous work we studied the band structure and other properties of single-layer and bilayer graphene (Barbier *et al.*, 2008, 2009*b*) in the presence of one-dimensional (1D) periodic potential, i.e., a superlattice (SL). SLs are known to be useful in altering the band structure of materials and thereby broadening their technological applicability.

The already peculiar, cone-shaped band structure of single-layer graphene can be drastically changed in a SL. An interesting feature is that for certain SL parameters the carriers are restricted to move along one direction, i.e. they are collimated (Park *et al.*, 2009*a*). Furthermore, it was found that for other parameters of the SL instead of the single-valley (the K or K'-point) Dirac cone, "extra Dirac points" appeared at the Fermi level in addition to the original one (Ho *et al.*, 2009). The latter extra Dirac points are interesting because of their accompagning zero modes (Brey & Fertig, 2009) and their influence on many physical properties such as the density of states (Ho *et al.*, 2009), the conductivity (Barbier *et al.*, 2010; Wang & Zhu, 2010), and the Landau levels upon applying a magnetic field (Park *et al.*, 2009*b*; Sun *et al.*, 2010).

One can also obtain "extra Dirac points" in bilayer graphene SLs. The possibility of locally altering the gap (Castro *et al.*, 2007) of bilayer graphene by applying a bias is another way of tuning the band structure. In this review we classify these SLs in four types. Another interesting result of applying a bias locally is that sign flips of the bias introduce bound states along the interfaces (Martin *et al.*, 2008; Martinez *et al.*, 2009). These bound states break the time reversal symmetry and are distinct for the two K and K' valleys; this opens up perspectives for valley-filter devices (San-Jose *et al.*, 2009).

In this review we will use the following methods to describe our findings. For both single-layer and bilayer graphene we will use the nearest neighbour, tight-binding Hamiltonian in the continuum approximation, and restrict ourselves to the electronic structure in the neighbourhood of the K point. We then apply the transfer-matrix method to study the spectrum of and transmission through various potential barrier structures, which we approximate by piecewise constant potentials. We consider structures with a finite number of barriers and SLs.

We will study ballistic transport in systems with a finite number of barriers using the two-probe Landauer conductance while in a SL (infinite number of barriers) we will evaluate the spectrum and the diffusive conductivity, i.e., we will study non-ballistic transport.

The work is organized as follows. In Sec. 2 we investigate various aspects of ballistic transport through a finite number of barriers on single-layer graphene as well as the spectrum of SLs, with emphasis on collimation and extra Dirac points and their influence on non-ballistic transport. In Sec. 3 we carry on the same studies, whenever possible, on bilayer graphene. In addition, we consider various types

of band alignments in the presence of a bias that can lead to different types of heterostructures and SLs. We make a summary and concluding remarks in Sec. 4.

2. Single-layer graphene

We describe the electronic structure of an infinitely large, flat graphene flake by the nearest-neighbour tight-binding model and consider wave vectors close to the K point. The relevant Hamiltonian in the continuum approximation is $\mathcal{H} = v_F \boldsymbol{\sigma} \cdot \hat{\mathbf{p}} + V\mathbb{1} + mv_F^2 \sigma_z$, with $\hat{\mathbf{p}}$ the momentum operator, V the potential, $\mathbb{1}$ the 2×2 unit matrix, $\boldsymbol{\sigma} = (\sigma_x \sigma_y)$, σ_z the Pauli-matrices and $v_F \approx 10^6 m/s$ the Fermi velocity. Explicitly $\mathcal{H}$ is given by

$$\mathcal{H} = \begin{pmatrix} V + mv_F^2 & -\mathrm{i}v_F\hbar(\partial_x - \mathrm{i}\partial_y) \\ -\mathrm{i}v_F\hbar(\partial_x + \mathrm{i}\partial_y) & V - mv_F^2 \end{pmatrix}. \tag{2.1}$$

The mass term is in principle zero in the nearest-neighbour, tight-binding model but due to interaction with a substrate (Giovannetti *et al.*, 2007) an effective mass term can be induced and results in the opening of an energy gap. Recently there have been proposals to induce an energy gap in single-layer graphene, and it is appropriate that we consider this mass term where relevant. In the presence of a 1D rectangular potential $V(x)$, such as the one shown in Fig. 1, the equation $(\mathcal{H} - E)\psi = 0$ admits (right- and left-travelling) plane wave solutions of the form $\psi_{l,r}(x)e^{ik_y y}$ with

$$\psi_r(x) = \begin{pmatrix} \varepsilon + \mu \\ \lambda + \mathrm{i}k_y \end{pmatrix} e^{\mathrm{i}\lambda x}, \; \psi_l(x) = \begin{pmatrix} \varepsilon + \mu \\ -\lambda + \mathrm{i}k_y \end{pmatrix} e^{-\mathrm{i}\lambda x}, \tag{2.2}$$

here $\lambda = [(\varepsilon - u(x))^2 - k_y^2 - \mu^2]^{1/2}$ is the x component of the wave vector, $\varepsilon = EL/\hbar v_F$, $u(x) = V(x)L/\hbar v_F$, and $\mu = mv_F L/\hbar$. The dimensionless parameters ε, $u(x)$ and μ scale with the characteristic length L of the potential barrier structure. For the single or double barrier system this L will be equal to the barrier width while for a SL it will be its period. Neglecting the mass term one rewrites Eq. (2.2) in the simpler form

$$\psi_r(x) = \begin{pmatrix} 1 \\ se^{\mathrm{i}\phi} \end{pmatrix} e^{\mathrm{i}\lambda x}, \quad \psi_l(x) = \begin{pmatrix} 1 \\ -se^{-\mathrm{i}\phi} \end{pmatrix} e^{-\mathrm{i}\lambda x}, \tag{2.3}$$

with $\lambda = [(\varepsilon - u(x))^2 - k_y^2]^{1/2}$, $\tan\phi = k_y/\lambda$, and $s = \mathrm{sgn}(\varepsilon - u(x))$.

(a) A single or double barrier

The model barriers and wells we consider are shown in Fig. 1(a). It is interesting to look at the tunneling through such barriers, which was previously studied by (Katsnelson *et al.*, 2006) for a single barrier. This was later extended to massive electrons with spatially varying mass (Gomes & Peres, 2008).

Transmission. To find the transmission T through a square-barrier structure one first observes that the wave function in the jth region $\psi_j(x)$ of the constant potential V_j is given by a superposition of the eigenstates given by Eq. (2.2),

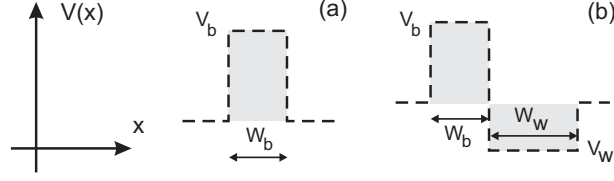$$\psi_j(x) = A_j \psi_{r_j} + B_j \psi_{l_j}. \tag{2.4}$$

Figure 1. (a) A 1D potential barrier of height V_b and width W_b. (b) A single unit of a potential well next to a potential barrier.

The wave function should be continuous at the interfaces. This boundary condition gives the transfer matrix $\mathcal{N}_j$ relating the coefficients A_j and B_j of region j with those of the region $j+1$ in the manner

$$\begin{pmatrix} A_j \\ B_j \end{pmatrix} = \mathcal{N}_{j+1} \begin{pmatrix} A_{j+1} \\ B_{j+1} \end{pmatrix}. \tag{2.5}$$

By employing the transfer matrix at each potential step we obtain, after n steps, the relation

$$\begin{pmatrix} A_0 \\ B_0 \end{pmatrix} = \prod_{j=1}^{n} \mathcal{N}_j \begin{pmatrix} A_n \\ B_n \end{pmatrix}. \tag{2.6}$$

In the region to the left of the barrier we assume $A_0 = 1$ and denote by $B_0 = r$ the reflection amplitude. Likewise, to the right of the nth barrier we have $B_n = 0$ and denote by $A_n = t$ the transmission amplitude.

The transmission probability T can be expressed as the ratio of the transmitted current density j_x over the incident one, where $j_x = v_F \psi^\dagger \sigma_x \psi$. This results in $T = (\lambda'/\lambda)|t|^2$, with λ'/λ the ratio between the wave vector λ' to the right and λ to the left of the barrier. If the potential to the right and left of the barrier is the same we have $\lambda' = \lambda$. For a single barrier the transmission amplitude is given by $T = |t|^2 = |N_{11}|^{-1}$, with N_{ij} the elements of the transfer matrix $\mathcal{N}$. Explicitly, t can be written as

$$1/t = \cos(\lambda_b W_b) - iQ \sin(\lambda_b W_b),$$
$$Q = (\varepsilon_0 \varepsilon_b - k_y^2 - \mu_0 \mu_b)/\lambda_0 \lambda_b; \tag{2.7}$$

the indices 0 and b refer, respectively, to the region outside and inside the barrier and $\varepsilon_b = \varepsilon - u$. A contour plot of the transmission is shown in Fig. 2(a). We clearly see: 1) $T = 1$ for $\phi = 0$ which is the well-known Klein tunneling, and 2) strong resonances, in particular for $E < 0$, when $\lambda_b W_b = n\pi$, which describe hole scattering above a potential well.

In the limit of a very thin and high barrier, one can model it by a δ-function barrier $V(x)/\hbar v_F = P\delta(x)$. Using Eq. (2.7) for t gives (Barbier *et al.*, 2009a)

$$T = 1/[1 + \sin^2 P \tan^2 \phi], \tag{2.8}$$

with $\tan \phi = k_y/\lambda_0$ the angle of incidence. Notice that this transmission is independent of the energy and is a *periodic* function of P. The latter is very different from the non-relativistic case where T is a decreasing function of P. A contour plot of the transmission is shown in Fig. 2(b) and $T = 1$ for $\phi \approx 0$ which is nothing else than Klein tunneling. Notice also the symmetry $T(\pi - P) = T(P)$.
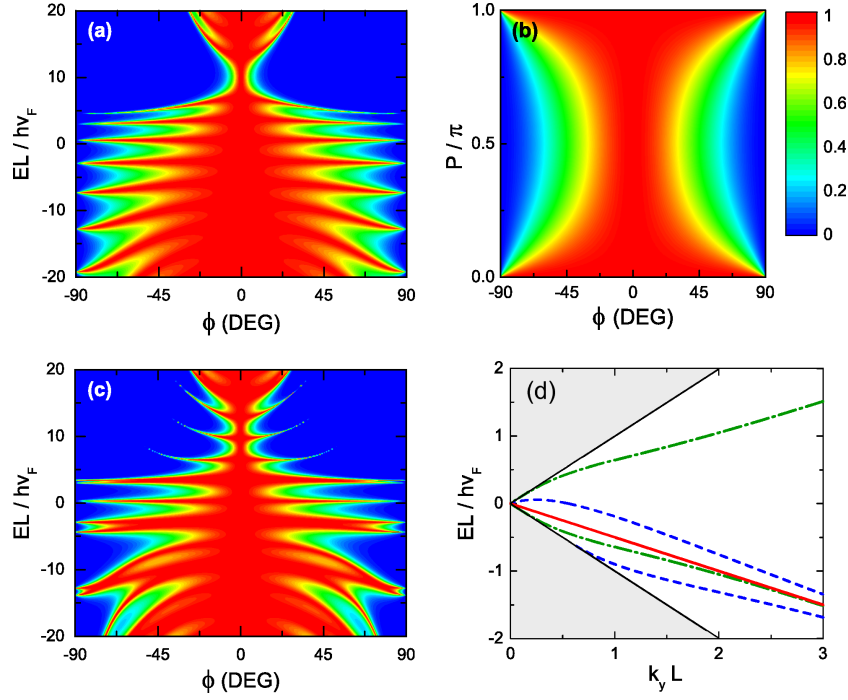
Figure 2. (a) Contour plot of the transmission through a single barrier with $\mu = 0$, $W_b = L$, and $u_b = 10$. (b) As in (a) for a single δ-function barrier with $\mu = 0$ and $u(x) = P\delta(x)$; the transmission is independent of the energy. (c) As in (a) for two barriers with $\mu = 0$, $u_b = 10$, $u_w = 0$, $W_b = 0.5L$, and $W_w = L$. (d) Spectrum of the bound states vs k_y for a single ($L = 1$, solid red line), two parallel (dashed blue curves), and two anti-parallel (green dash-dotted curves) δ-function barriers (L is the inter-barrier distance).

For two barriers the system becomes a resonant structure, for which it was found that the resonances in the transmission depend mostly on the width W_w of the well between the barriers (Pereira Jr *et al.*, 2007*a*). A plot of the transmission is shown in Fig. 2(c). In the limit of two parallel δ-function barriers of equal strength P we obtain the transmission

$$T = \left[1 + \tan^2\phi(\cos\lambda_0 \sin 2P - 2s \sin\lambda_0 \sin^2 P/\cos\phi)^2\right]^{-1}. \qquad (2.9)$$

The case of two anti-parallel δ-function barriers of equal strength is also interesting. The relevant transmission is

$$T = \left[\cos^2\lambda_0 + \sin^2\lambda_0(1 - \sin^2\phi\cos 2P)^2/\cos^4\phi\right]^{-1}. \qquad (2.10)$$

Conductance. The two-terminal conductance is given by

$$G(E_F) = G_0 \int_{-\pi/2}^{\pi/2} T(E_F, \phi)\cos\phi \, d\phi, \qquad (2.11)$$

with $G_0 = 2E_F L_y e^2/(v_F h^2)$ for single-layer graphene, and L_y the width of the system. For a single and double barrier, the transmission through which is plotted

in Fig. 2(a) and 2(c), the conductance G is shown in Fig. 3(b) and exhibits multiple resonances despite the integration over the angle ϕ.

Taking the limit of a δ-function barrier leads to G periodic in P and given by

$$G/G_0 = 2\big[1 - \text{artanh}(\cos P)\sin P \tan P\big]/\cos^2 P. \qquad (2.12)$$
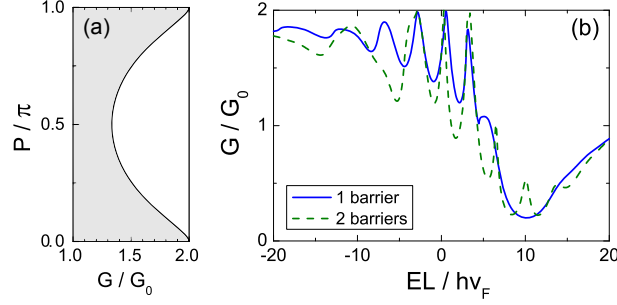
For one period G is shown in Fig. 3(a).

Figure 3. (a) Conductance G vs strength P of a δ-function barrier in single-layer graphene; the conductance is independent of the energy. (b) Conductance G vs energy for the single (solid blue curve) and double (dashed green curve) square barrier of Fig. 2(a) and 2(c).

Bound states. For $k_y^2 + \mu_0^2 > \varepsilon^2$ the wave function outside the barrier (well) becomes an exponentially decaying function of x, $\psi(x) \propto \exp\{\pm|k_x|x\}$ with $|k_x| = [k_y^2 + \mu_0^2 - \varepsilon^2]^{1/2}$. Localized states form near the barrier boundaries (Pereira Jr *et al.*, 2006); however, they are propagating freely along the y-direction. The spectrum of these bound states can be found by setting the determinant of the transfer matrix equal to zero. For a single potential barrier (well) it is given by the solution of the transcendental equation

$$|\lambda_0|\lambda_b \cos(\lambda_b W_b) + (k_y^2 + \mu_0\mu_b - \varepsilon(\varepsilon - u))\sin(\lambda_b W_b) = 0. \qquad (2.13)$$

In Fig. 4(b) these bound states are shown, as a function of k_y, by the dashed blue (red) curves.

An interesting structure to study is that of a potential barrier next to a well but with average potential equal to zero, considered by (Arovas *et al.*, 2010). This is the unit cell (shown in Fig. 1(b)) of the SL we will use in Sec. 3 where extra Dirac points will be found. In Fig. 4(a) the Dirac cone outside the barrier is shown as a grey area, inside this region there are no bound states. Superimposed are grey lines corresponding to the edges of the Dirac cones inside the well and barrier that divide the (E, k_y) plane into four regions. Region I corresponds to propagating states inside both the barrier and well while region II (III) corresponds to propagating states only inside the well (barrier). In region IV no propagating modes are possible, neither in the barrier nor in the well. For high thin barriers, region I will become a thin area adjacent to the upper cone, converging to the dark green line in the limit of a δ-function barrier. Figure 4(b) shows that the bound states of this structure are composed of the ones of a single barrier and those of a single well. Anticrossings take place where the bands otherwise would cross. The resulting spectrum is clearly a starter of the spectrum of a SL shown in Fig. 4(d).
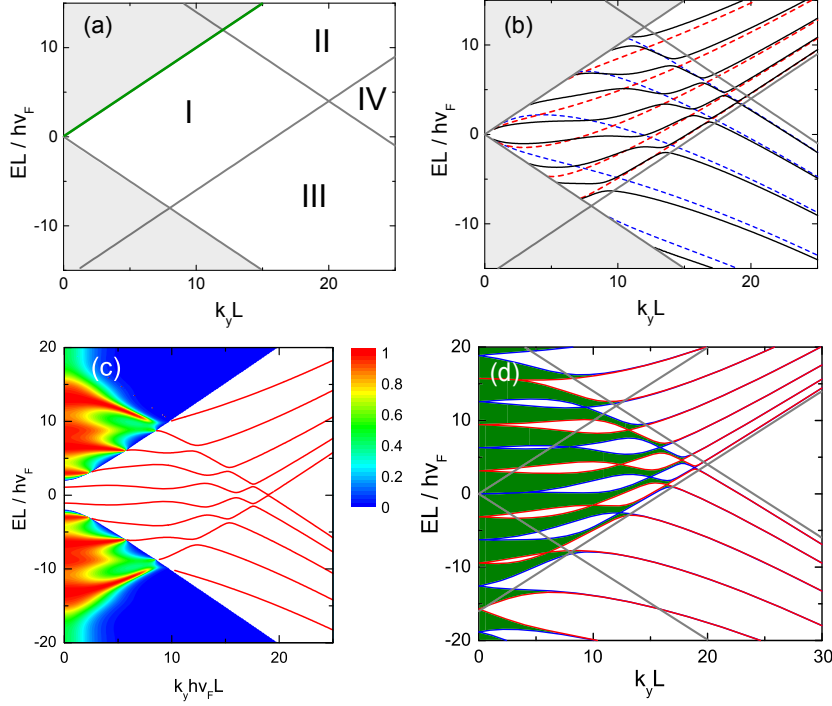
Figure 4. (a) Four different regions for a single unit of Fig. 1(b) with $u_b = 24$, $u_w = 16$, $W_b = 0.4$ and $W_w = 0.6$. The green line corresponds to region I in the limit of a δ-function barrier. (b) Bound states for a single barrier (dashed blue curves) and well (dashed red curves) and the combined barrier-well unit (black curves). (c) Contour plot of the transmission through a unit with $\mu = 2$, $u_b = -u_w = 20$ and $W_b = W_w = 0.5$; the red curves show the bound states. (d) Spectrum of a SL whose unit cell is shown in Fig. 1(b), for $k_x = 0$ (blue curves) and $k_x L = \pi/2$ (red curves).

In the limit of δ-function barriers and wells the expressions for the dispersion relation are strongly simplified by setting $\mu = 0$ in all regions. For a single δ-function barrier the bound state is given by

$$\varepsilon = \text{sgn}(\sin P)|k_y|\cos P, \tag{2.14}$$

which is a straight line with a reduced group velocity v_y; the result is shown in Fig. 2(d) by the red curve. Comparing with the single-barrier case we notice that due to the periodicity in P, the δ-function barrier can act as a barrier or as a well depending on the value of P.

For two δ-function barriers there are two important cases: the parallel and the anti-parallel case. For parallel barriers one finds an implicit equation for the energy

$$|\lambda' \cos P + \varepsilon \sin P| = |\mathrm{e}^{-\lambda'} k_y \sin P|, \tag{2.15}$$

where $\lambda' = |\lambda_0|$, while for anti-parallel barriers one obtains

$$k_y^2 \sin^2 P = \lambda'^2/(1 - \mathrm{e}^{-2\lambda'}). \tag{2.16}$$

For two (anti-)parallel δ-function barriers we have, for each fixed k_y and P, two energy values $\pm\varepsilon$, and therefore two bound states. In both cases, for $P = n\pi$ the spectrum is simplified to the one in the absence of any potential $\varepsilon = \pm|k_y|$. In Fig. 2(d) the bound states for double (anti-)parallel δ-function barriers are shown, as a function of k_yL, by the dashed blue (dash-dotted green) curves. For anti-parallel barriers we see that there is a symmetry around $E = 0$, which is absent when the barriers are parallel.

(b) *Superlattice*

Now we will consider the system of a superlattice with a corresponding 1D periodic potential, with square barriers, given by

$$V(x) = V_0 \sum_{j=-\infty}^{\infty} [\Theta(x - jL) - \Theta(x - jL - W_b)]. \qquad (2.17)$$

with $\Theta(x)$ the step function. The corresponding wave function is a Bloch function and satisfies the periodicity condition $\psi(L) = \psi(0)\exp(ik_x)$, with k_x now the Bloch phase. Using this relation together with the transfer matrix for a single unit $\psi(L) = \mathcal{M}\psi(0)$ leads to the condition

$$\det[\mathcal{M} - \exp(ik_x)] = 0. \qquad (2.18)$$

This gives the transcendental equation

$$\cos k_x = \cos \lambda_w W_w \cos \lambda_b W_b - Q \sin \lambda_w W_w \sin \lambda_b W_b, \qquad (2.19)$$

from which we obtain the energy spectrum of the system. In Eq. (2.19) we used the following notation:

$$\varepsilon_w = \varepsilon + uW_b, \quad \varepsilon_b = \varepsilon - uW_w, \quad u = V_0 L/\hbar v_F, \quad W_{b,w} \to W_{b,w}/L,$$

$$\lambda_w = [\varepsilon_w^2 - k_y^2 - \mu_w^2]^{1/2}, \quad \lambda_b = [\varepsilon_b^2 - k_y^2 - \mu_b^2]^{1/2}, \quad Q = (\varepsilon_w\varepsilon_b - k_y^2 - \mu_b\mu_w)/\lambda_w\lambda_b.$$

Numerical results for the dispersion relation $E(k_y)$ are shown in Fig. 4(d). We see the appearance of bands (green areas) which for large k_y values collapse into the bound states (where the red and blue curves meet) while the charge carriers move freely along the y direction.

(c) *Collimation and extra Dirac points*

As shown by various studies, carriers in graphene SLs exhibit several interesting pecularities that result from the particular electronic SL band structure. In a 1D SL it was found that the spectrum can be altered anisotropically (Park *et al.*, 2008*a*; Bliokh *et al.*, 2009). Moreover, this anisotropy can be made very large such that for a broad region in **k** space the spectrum is dispersionless in one direction, and thus electrons are collimated along the other direction (Park *et al.*, 2009*a*). Even more intriguing was the ability to split off "extra Dirac points" (Ho *et al.*, 2009) with accompanying zero modes (Brey & Fertig, 2009) which move away from the K point along the k_y direction with increasing potential strength. Here we will describe these phenomena for a SL of square potential barriers.

We start by describing the collimation as done by (Park *et al.*, 2009*a*); subsequently we will find the conditions on the parameters of the SL for which a collimation appears. It turns out that they are the same as those needed to create a pair of extra Dirac points.
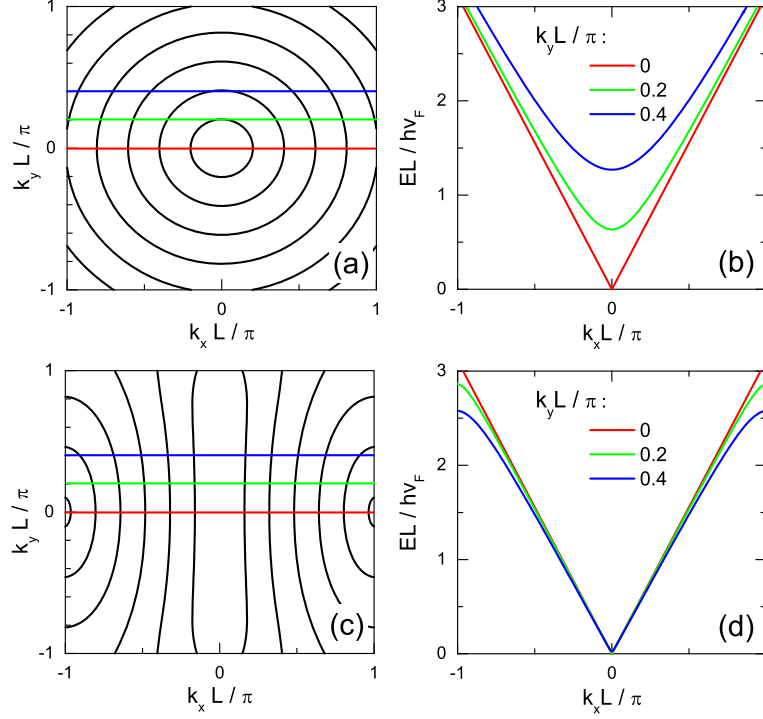

Figure 5. The lowest conduction band of the spectrum of graphene near the K point in the absence of SL potential (a), (b) and in its presence (c), (d) with $u = 4\pi$. (a) and (c) are contour plots of the conduction band with a contour step of 0.5 $\hbar v_F/L$. (b) and (d) show slices along constant $k_y L = 0, 0.2, 0.4\pi$.

Following (Park *et al.*, 2009*a*) the condition for collimation to occur is $\int_{BZ} e^{is\hat{s}\alpha(x)} = 0$, where the function $\alpha(x) = 2\int_0^x u(x')\mathrm{d}x'$ embodies the influence of the potential, $s = \mathrm{sign}(\varepsilon)$ and $\hat{s} = \mathrm{sign}(k_x)$. For a symmetric rectangular lattice this corresponds to $u/4 = n\pi$. The spectrum for the lowest energy bands is then given by (Park *et al.*, 2008*b*)

$$\varepsilon \approx \pm\left[k_x^2 + |f_l|^2 k_y^2\right]^{1/2} + \pi l/L \tag{2.20}$$

with f_l being the coefficients of the Fourier expansion $e^{i\alpha(x)} = \sum_{l=-\infty}^{\infty} f_l e^{i2\pi lx/L}$. The coefficients f_l depend on the potential profile $V(x)$, with $|f_l| < 1$. For a symmetric SL of square barriers we have $f_l = u\sin(l\pi/2 - u/2)/(l^2 u^2 - u^2/4)$. The inequality $|f_l| < 1$ implies a group velocity in the y direction $v_y < v_F$ which can be seen from Eq. (2.20).

In Fig. 5(b),(d) we show the dispersion relation E vs k_x for $u = 4\pi$ at constant k_y. As can be seen, when a SL is present in most of the Brillouin zone the spectrum, partially shown in (c), is nearly independent of k_y. That is, we have collimation

of an electron beam along the SL axis. The condition $u = V_0 L / \hbar v_F = 4n\pi$ shows that altering the period of the SL *or* the potential height of the barriers is sufficient to produce collimation. This makes a SL a versatile tool for tuning the spectrum. Comparing with Figs. 5(a), (b) we see that the cone-shaped spectrum for $u = 0$, is transformed into a wedge-shaped spectrum (Park *et al.*, 2009*a*).

We will compare this result now with an other approximate result for the spectrum, where we suppose ε small instead of k_y small. We start with the transcendental equation (2.19). As we are interested in an analytical approximate expression for the spectrum, we choose to expand the dispersion relation around $\varepsilon = 0$ up to second order in ε. The resulting spectrum is

$$\varepsilon_\pm = \pm \left[\frac{4|a^2|^2 \left[k_y^2 \sin^2(a/2) + a^2 \sin^2(k_x/2) \right]}{k_y^4 a \sin a + a^2 u^4/16 - 2k_y^2 u^2 \sin^2(a/2)} \right]^{1/2}, \qquad (2.21)$$

with $a = [u^2/4 - k_y^2]^{1/2}$. In order to compare this spectrum with that by (Park *et al.*, 2009*a*), we expand Eq. (2.19) for small $\mathbf{k}$ and ε; this leads to

$$\varepsilon \approx \pm \left[k_x^2 + k_y^2 \sin^2(u/4)/(u/4)^2 \right]^{1/2}. \qquad (2.22)$$

This spectrum has the form of an anisotropic cone and corresponds to that of Eq. (2.20) for $l = 0$ (higher l correspond to higher energy bands). In Fig. 6(a), (b) we see that the cone-shaped spectrum in (a), for $u = 0$, is transformed into a anisotropic spectrum in (b), for $u = 4.5\pi$, having peculiar extra Dirac points. These extra Dirac points cannot be described by a spectrum having an anisotropic cone-shape, therefore we compare the two approximate spectra. In Fig. 6(c), (d) we show how Eq. (2.21)) and Eq. (2.22) differ from the "exact" numerically obtained spectrum. From this figure one can see that Eq. (2.21) describes the lowest bands rather well for $\varepsilon < 1$, while Eq. (2.22) is sufficient to describe the spectrum near the Dirac point. The former equation will be usefull when describing the spectrum near the extra Dirac points and we will use it to obtain the velocity.

We now move on to another important feature of the spectrum, the extra Dirac points first obtained by (Ho *et al.*, 2009) using tight-binding calculations. These extra Dirac points are found as the zero-energy solutions of the dispersion relation in Eq. (2.19) for zero energy (Barbier *et al.*, 2010).

In order to find the location of the Dirac points we assume $k_x = 0$, $\varepsilon = 0$, $\mu_b = \mu_w = 0$, and consider the special case of $W_b = W_w = 1/2$ in Eq. (2.19). The resulting equation

$$1 = \cos^2 \lambda/2 + \left[(u^2/4 + k_y^2)/(u^2/4 - k_y^2) \right] \sin^2 \lambda/2, \qquad (2.23)$$

has solutions for $u^2/4 - k_y^2 = u^2/4 + k_y^2$ or $\sin^2 \lambda/2 = 0$. This determines the values of $k_y = 0$ (at the Dirac points) as

$$k_{y,j\pm} = \pm\sqrt{\frac{u^2}{4} - 4j^2\pi^2}; \qquad (2.24)$$

the extra Dirac points are for $j \neq 0$. For a SL spectrum symmetric around zero energy, the extra Dirac points are at $\varepsilon = 0$. We expect from the considerations of Sec. 2(b) (and Fig. 4(b)) that for unequal barrier and well widths this will no longer

be true. Indeed, in such a case the extra Dirac points shift in energy, as seen in Fig. 4(d), and their position in the spectrum is given, for $k_x = 0$, by (Barbier *et al.*, 2010)

$$\varepsilon_{j,m} = \frac{u}{2}(1 - 2W_b) + \frac{\pi^2}{2u}\left(\frac{j^2}{W_w^2} - \frac{(j+2m)^2}{W_b^2}\right),$$

$$k_{y_{j,m}} = \pm\left[(\varepsilon_{j,m} + uW_b)^2 - (j\pi/W_w)^2\right]^{1/2},$$

(2.25)

where j and m are integers, and $m \neq 0$ corresponds to higher and lower crossing points. Also, perturbing the potential with an asymmetric term, as done by (Park *et al.*, 2009*b*), leads to qualitatively similar results.
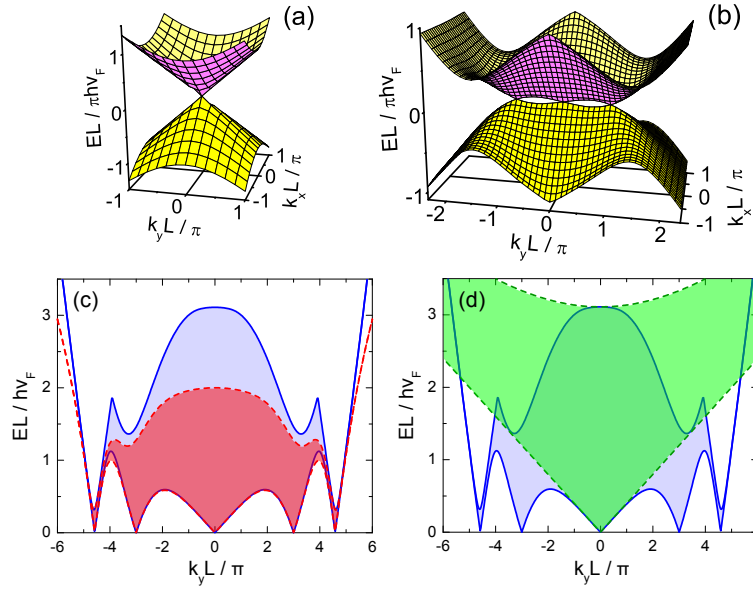

Figure 6. The spectrum of graphene near the K point in the absence of a SL (a) and in its presence (b) with $u = 4.5\pi$. (c) and (d) The SL spectrum with $u = 10\pi$, the lowest conduction bands are coloured in cyan, red, and green for, respectively, the exact, and the approximations given by (c) Eq. (2.21) and (d) Eq. (2.22), respectively. The approximate spectra are delimited by the dashed curves.

An investigation of the group velocity near the (extra) Dirac points is appropriate for understanding the transport of carriers in the energy bands close to zero energy. Near the extra Dirac points the group velocity tends to renormalise differently as compared to the original Dirac point. Near them $\mathbf{v}$ is oriented along the y direction, while near the latter one $\mathbf{v}$ is oriented along the x direction (Ho *et al.*, 2009). The group velocity near the extra Dirac points can be calculated from Eq. (2.21). At the jth extra Dirac point the magnitude of the velocity $\mathbf{v}/v_F = (\partial\varepsilon/\partial k_x, \partial\varepsilon/\partial k_y)$ is given by

$$v_x/v_F = 16\pi^2 j^2 \cos(k_x/2)/u^2$$

$$v_y/v_F = (u^2/4 - 4j^2\pi^2)/u^2,$$

(2.26)

while at the main Dirac point it is given by $v_x/v_F = 1$ and $v_y/v_F = 4\sin(u/4)/u$. The dependence of the velocity components on the strength of the potential barriers is shown in Fig. 7. From this figure we observe that new extra Dirac points emerge upon increasing $u = V_0 L/\hbar v_F$ (consistent with Eq. (2.24)) and v_x decreases while v_y increases. The Dirac point itself, however, shows a different behaviour upon increasing u, namely $v_x = v_F$ constant, and v_y is here a globally decaying function showing $v_y = 0$ for periodic values of u, $u = 4n\pi$, with n a nonzero positive integer.
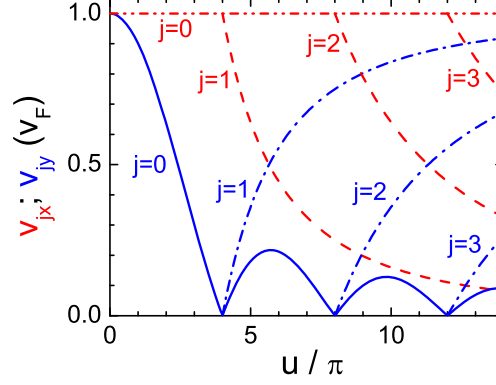

Figure 7. The group velocity components v_y and v_x at the Dirac point $j = 0$ (shown, respectively, by the solid blue and the dot-dot-dashed red curve), and at the extra Dirac points $j = 1, 2, 3$ (shown, respectively, by the dot-dashed blue and the dashed red curves) as a function of the barrier parameter $u = V_0 L/\hbar v_F$.

Conductivity. We now turn to the transport properties of a SL and look at the influence of these extra Dirac points on the conductivity. The diffusive dc conductivity $\sigma_{\mu\nu}$ for the SL system can be readily calculated from the spectrum if we assume a nearly constant relaxation time $\tau(E_F) \equiv \tau_F$. It is given by (Charbonneau *et al.*, 1982)

$$\sigma_{\mu\nu}(E_F) = \frac{e^2 \beta \tau_F}{A} \sum_{n,\mathbf{k}} v_{n\mu} v_{n\nu} f_{n\mathbf{k}}(1 - f_{n\mathbf{k}}), \qquad (2.27)$$

with A the area of the system, n the energy band index, $\mu, \nu = x, y$, and $f_{n\mathbf{k}} = 1/[\exp(\beta(E_F - E_{n\mathbf{k}})) + 1]$ the equilibrium Fermi-Dirac distribution function; $\beta = 1/k_B T$ and the temperature enters the results through the dimensionless value for β which is $\beta = \hbar v_F/k_B T L = 20$.

For comparison we first look at the conductivity tensor at zero temperature and in the absence of a SL. For single-layer graphene the conductivity is given by

$$\sigma_{\mu\mu}(\varepsilon_F)/\sigma_0 = \varepsilon_F/4\pi \qquad (2.28)$$

with $\sigma_0 = e^2/\hbar$,

In Figs. 8(a), (b) the conductivities σ_{xx} and σ_{yy} are shown for a SL as functions of the energy. Notice that for small energies the slope of the conductivity σ_{yy} is tunable to a large extent by altering the parameter u of the SL. The dashed blue curves correspond to $u = 4\pi$ and the rather flat dispersion in the y direction for

the lowest conduction band (see Fig. 5(c,d)) translates to a small σ_{yy} (for energies $EL/\hbar v_F < 1$) compared to the conductivity in the absence of a SL. The solid red curves on the other hand correspond to $u = 6\pi$ and due to the extra Dirac points, which have a rather flat dispersion in the x direction (Ho *et al.*, 2009), the conductivity σ_{yy} is large.
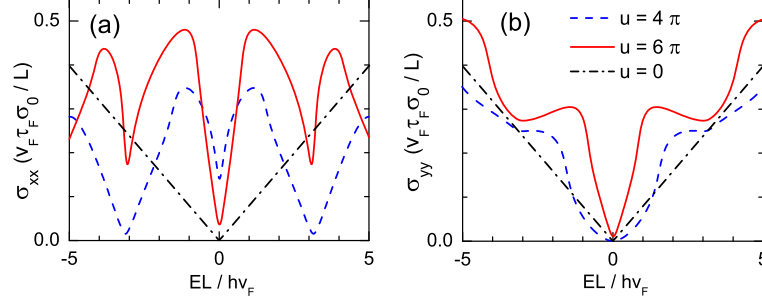

Figure 8. (Color online) Conductivities, σ_{xx} in (a) and σ_{yy} in (b), vs Fermi energy for a SL on single-layer graphene with $u = 4\pi$ and 6π for, respectively, the blue dashed and red solid curves. In both cases $W_b = W_w = 0.5$. The dash-dotted black curves show the conductivities in the absence of the SL potential, $\sigma_{xx} = \sigma_{yy} = \varepsilon_F \sigma_0/4\pi$.
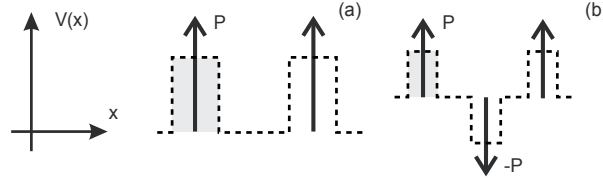
(d) Dirac lines

Figure 9. (a) Schematics of Kronig-Penney SL on single-layer graphene. (b) Extended Kronig-Penney SL.

In an effort to simplify the expressions for the dispersion relation we replace, as we did for the few-barrier structures, the SL barriers by δ-function barriers. The square SL potential is then approximated by

$$V(x) = P \sum_{j=-\infty}^{\infty} \delta(x - jL). \tag{2.29}$$

This potential leads to the dispersion relation

$$\cos k_x = \cos \lambda \cos P + (\varepsilon/\lambda) \sin \lambda \sin P, \tag{2.30}$$

which is *periodic* in P. This is in sharp contrast with that for standard electrons which is *not periodic* in P and which in our notation reads

$$\cos k_x = \cos \lambda' + (\mu P/\lambda') \sin \lambda', \tag{2.31}$$

where $\mu = m v_F L / \hbar$ and $\lambda' = [2\mu\varepsilon - k_y^2]^{1/2}$. As can be seen from Fig. 10(a), the energy band near the Dirac point has the interesting property that it becomes nearly flat in k_x, forming a plane, for large k_y. The angle which the asymptotic plane makes with the zero-energy plane depends on P and the group velocity v_y corresponding to this asymptotic plane varies from $-v_F$ to v_F in each period $n\pi < P < (n+1)\pi$. Notice that no extra Dirac points are found and the reason is the same as that for the asymmetric SL potential, i.e., the extra Dirac points shift away from zero energy. Alternatively, we can try to shed some light by comparing with Sec. 2(b), where it is explained that the bound states for a single unit of the SL potential are similar to those of the combined single barrier and well. In the region where the bound states cross (denoted by I in Fig. 4(a)) anti-crossings occur and corresponding crossings in the SL spectrum (extra Dirac points) are expected. In the limit of a δ-function barrier this region is reduced to a line (the dark green line in Fig. 4(a)). This prevents anti-crossings from occurring and in this way no extra Dirac points are expected.
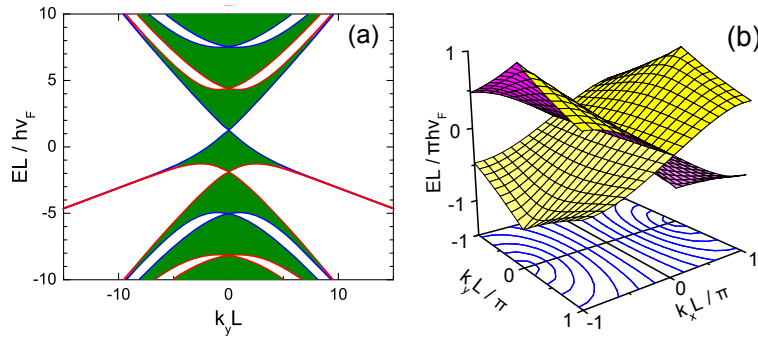

Figure 10. (a) Spectrum for a Kronig-Penney SL with $P = 0.4\pi$. The blue and red curves show, respectively, the $k_x = 0$ and $k_x = \pi/L$ results which delimit the energy bands (green coloured regions). (b) Spectrum for an extended Kronig-Penney SL with $P = \pi/2$. Notice that the Dirac point has become a Dirac line.

Extended Kronig-Penney model. To re-establish the symmetry between electrons and holes, as in the case of square barriers with $W_b = W_w$, we can use alternating-in-sign δ-function barriers. The unit cell of the periodic potential contains one such barrier up, at $x = 0$, followed by a barrier down, at $x = L/2$, see Fig. 9(b). The potential is given by

$$V(x) = P \sum_{j=-\infty}^{\infty} [\delta(x - jL) - \delta(x - jL - L/2)], \tag{2.32}$$

and is the asymptotic limit of the potential shown in Fig. 1(b). The resulting transfer matrix leads to the dispersion relation

$$\cos k_x = \cos \lambda - (2k_y^2/\lambda^2) \sin^2(\lambda/2) \sin^2 P. \tag{2.33}$$

This dispersion relation is *periodic* in P. As shown in Fig. 10(b) no extra Dirac points occur, but for the particular case of $P = (n + 1/2)\pi$, n an integer, the

spectrum shows an interesting feature: for all k_y we see that Eq. (2.33) has a solution with $\varepsilon = k_x = 0$, which means the Dirac point at $k_x = k_y = 0$ turned into a Dirac line along the k_y axis. If we take k_y not too large (of the order of k_x), this spectrum has a wedge structure as was also found for rectangular SLs. For $k_y \to \infty$, though, the spectrum becomes a horizontal plane situated at $\varepsilon = 0$. We can generalize this model by taking the distance W between the two barriers of the unit cell not equal to $L/2$. This was done by (Ramizani Masir *et al.*, 2010, unpublished work). They found an approximate analytic expression for the dispersion given by

$$\varepsilon \approx [k_x^2 + F k_y^2]^{1/2}, \qquad F = W^2 + (L-W)^2 + 2W(L-W)\cos(2P). \qquad (2.34)$$

This dispersion has the shape of an anisotropic cone with a renormalized velocity in the y direction. Comparing with Eqs. (2.20) and (2.22), we observe that the condition for collimation and the velocity renormalization in the y direction is quite different for square barriers. For instance, in the extended KP model, with $W = L/2$, we find $v_y/v_F = |\cos P|$ while for square barriers the result is $v_y/v_F = \sin(u/4)/(u/4)$. The latter means that if we consider $P \equiv u/4$, the velocity in the y direction is maximum $v_y = v_F$ for $P = (1/2 + n)\pi$ in the extended KP model while for square barriers $v_y = 0$ at these points.

3. Bilayer graphene

We now turn to bilayer graphene and use again the nearest-neighbour, tight-binding Hamiltonian in the continuum approximation with $\mathbf{k}$ close to the K point. If we include a potential difference between the two layers, the Hamiltonian is given by

$$\mathcal{H} = \begin{pmatrix} U_1 & v_F \pi & t_\perp & 0 \\ v_F \pi^\dagger & U_1 & 0 & 0 \\ t_\perp & 0 & U_2 & v_F \pi^\dagger \\ 0 & 0 & v_F \pi & U_2 \end{pmatrix}. \qquad (3.1)$$

Here U_1 and U_2 are the potentials on layers 1 and 2, respectively, $2\Delta = U_1 - U_2$ is the potential difference, and $t_\perp$ describes the coupling between the layers. The energy spectrum for free electrons is given by (McCann, 2006; Barbier *et al.*, 2009*b*)

$$\begin{aligned}
\varepsilon &= u_0 \pm \left[\Delta^2 + k^2 + \frac{t_\perp^2}{2} + (4\Delta^2 k^2 + k^2 t_\perp^2 + \frac{t_\perp^2}{4})^{1/2} \right]^{1/2}, \\
\varepsilon &= u_0 \pm \left[\Delta^2 + k^2 + \frac{t_\perp^2}{2} - (4\Delta^2 k^2 + k^2 t_\perp^2 + \frac{t_\perp^2}{4})^{1/2} \right]^{1/2},
\end{aligned} \qquad (3.2)$$

with $u_1 = u_0 + \Delta$ and $u_2 = u_0 - \Delta$. Contrary to Sec. 3 we use units in inverse distance, namely, $\varepsilon = E/\hbar v_F$, $u_j = U_j/\hbar v_F$, and $k = [\lambda^2 + k_y^2]^{1/2}$. This spectrum exhibits an energy gap that for $2\Delta \ll t_\perp$ equals the difference 2Δ between the conduction and valence band at the K point (McCann, 2006).

Solutions for this Hamiltonian are four-vectors ψ and for 1D potentials we can write $\psi(x,y) = \psi(x)\exp(ik_y y)$. If the potentials U_1 and U_2 do not vary in space, these solutions are of the form

$$\Psi_\pm(x) = \begin{pmatrix} 1 \\ f_\pm \\ h_\pm \\ g_\pm h_\pm \end{pmatrix} e^{\pm i\lambda x + ik_y y}, \qquad (3.3)$$

with $f_\pm = [-\mathrm{i}k_y \pm \lambda]/[\varepsilon' - \delta]$, $h_\pm = [(\varepsilon' - \delta)^2 - k_y^2 - \lambda^2]/[t_\perp(\varepsilon' - \delta)]$, and $g_\pm = [\mathrm{i}k_y \pm \lambda]/[\varepsilon' + \delta]$; the wave vector λ is given by

$$\lambda_\pm = \left[\varepsilon'^2 + \delta^2 - k_y{}^2 \pm \sqrt{4\varepsilon'^2\delta^2 + t_\perp^2(\varepsilon'^2 - \delta^2)} \right]^{1/2}. \qquad (3.4)$$

We will write $\lambda_+ = \alpha$ and $\lambda_- = \beta$.

(a) Tuning of the band offsets

It was shown before that using a 1D biasing, indicated in Figs. 11(a,b,c) by 2Δ, one can create three types of heterostructures in graphene (Dragoman *et al.*, 2010). A fourth type, where the energy gap is spatially kept constant but the bias periodically changes sign along the interfaces, can be introduced (see Fig. 11(d)). We characterize these heterostructures as follows:

1) **Type I:** The gate bias applied in the barrier regions is larger than in the well regions.

2) **Type II:** The gaps, not necessarily equal, are shifted in energy but they have an overlap as shown.

3) **Type III:** The gaps, not necessarily equal, are shifted in energy and have no overlap.

4) **Type IV:** The bias changes sign between successive barriers and wells but its magnitude remains constant.

Type IV structures have been shown to localize the wave function at the interfaces (Martin *et al.*, 2008; Martinez *et al.*, 2009). To understand the influence of such interfaces in this section we will separately investigate structures with such a single interface embedded by an anti-symmetric potential.
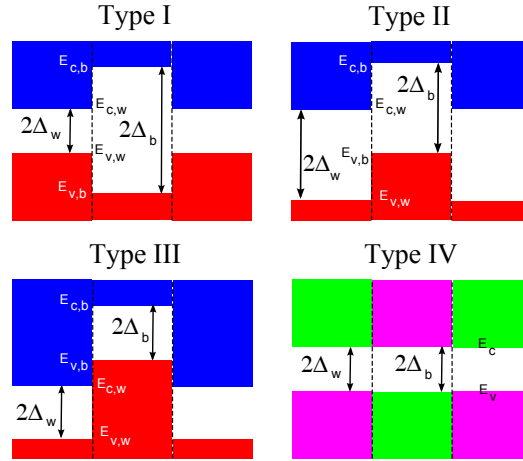

Figure 11. Four different types of band alignments in bilayer graphene. $E_{c,b}, E_{c,w}, E_{v,c}$, and $E_{v,b}$ denote the energies of the conduction (c) and valence (v) bands in the barrier (b) and well (w) regions. The corresponding gap is, respectively, $2\Delta_b$ and $2\Delta_w$.

To describe the transmission and bound states of some simple structures we notice that in the energy region of interest, i.e., for $|E| < t_\perp$, the eigenstates which are propagating are the ones with $\lambda = \alpha$. Accordingly, from now on we will assume that β is complex. In this way we can simply use the transfer-matrix approach of Sec. 2 in the transmission calculations. This leads to the relation

$$\begin{pmatrix} t \\ 0 \\ e_d \\ 0 \end{pmatrix} = \mathcal{N} \begin{pmatrix} 1 \\ r \\ 0 \\ e_g \end{pmatrix}. \tag{3.5}$$

Again the transmission is given by $T = |t|^2$.

For a single barrier the transmission in bilayer graphene is given by a complicated expression. Therefore, we will first look at a few limiting cases. First we assume a zero bias $\Delta = 0$ that corresponds to a particular case of type III heterostructures. In this case we slightly change the definition of the wave vectors: for $\Delta = 0$ we assume $\alpha(\beta) = [\varepsilon^2 + (-)\varepsilon t_\perp - k_y^2]^{1/2}$. If we restrict the motion along the x axis, by taking $k_y = 0$, and assume a bias $\Delta = 0$, then the transmission $T = |t|^2$ is given via

$$1/t = e^{i\alpha_0 D}[\cos(\alpha_b D) - iQ \sin(\alpha_b D)],$$
$$Q = \frac{1}{2}\left(\frac{\alpha_b \varepsilon_0}{\alpha_0 \varepsilon_b} + \frac{\alpha_0 \varepsilon_b}{\alpha_b \varepsilon_0}\right). \tag{3.6}$$

This expression depends only on the propagating wave vector α (β for $E < 0$) as propagating and localized states are decoupled in this approximation. This also means that one does not find any resonances in the transmission for energies in the barrier region, i.e., for $0 < \varepsilon < u$. Due to the coupling for nonzero k_y with the localized states, resonances in the transmission will occur (see Fig. 12). We can easily generalize this expression to account for the double barrier case under the same assumptions. With an inter-barrier distance W_w one obtains the transmission (Barbier *et al.*, 2009b) $T_d = |t_d|^2$ from

$$t_d = \frac{e^{i2\alpha_0(W_w+2W_b)}|t|^2 e^{i2\phi_t}}{1 - |r|^2 e^{i2\phi_r} e^{i2\alpha_0 W_w}}, \tag{3.7}$$

with $r = |r|e^{i\phi_r}$, and $t = |t|e^{i\phi_t}$, corresponding to the single barrier transmission and reflection amplitudes. In this case we do have resonances due to the well states; they occur for $e^{i2\phi_r} e^{i2\alpha_0 W_w} = 1$. As ϕ_r is independent of W_w, one obtains more resonances by increasing W_w.

For a single δ-function barrier with potential $V(x)/\hbar v_F = P\delta(x)$ under zero bias, we find the transmission amplitude

$$1/t = \cos P + i\mu \sin P + \frac{(\alpha - \beta)^2 k_y^2}{4\alpha\beta\varepsilon^2} \frac{\sin P}{\cot P + i\nu}, \tag{3.8}$$

where $\mu = (\varepsilon + 1/2)/\alpha$ and $\nu = (\varepsilon - 1/2)/\beta$. Notice that this formula is *periodic* in the strength of the barrier P as in the single-layer case.

For the general case we obtained numerical results for the transmission through various types of single and double barrier structures; they are shown in Fig. 13.
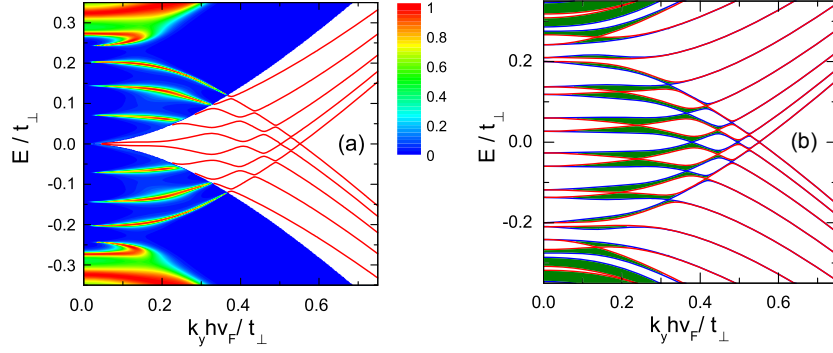
Figure 12. (a) Contour plot of the transmission for the potential of Fig. 1(b) in bilayer graphene with $W_b = W_w = 40$ nm, $V_b = -V_w = 100$ meV and zero bias. Bound states are shown by the red curves. (b) Spectrum for a SL whose unit is the potential structure of Fig. 1(b). Blue and red curves show, respectively, the $k_x = 0$ and $k_x = \pi/L$ results which delimit the energy bands (green coloured regions).

The different types of structures clearly lead to different behaviour of the tunnelling resonances.

An interesting structure to study is the fourth type of SLs shown in Fig. 11(d). To investigate the influence of the localized states (Martin *et al.*, 2008; Martinez *et al.*, 2009) on the transport properties we embed the anti-symmetric potential profile in a structure with unbiased layers.

Conductance At zero temperature G can be calculated from the transmission using Eq. (13) with $G_0 = (4e^2 L_y/2\pi h)\,(E_F^2 + t_\perp E_F)^{1/2}/\hbar v_F$ for bilayer graphene and L_y the width of the sample. The angle of incidence ϕ is given by $\tan\phi = k_y/\alpha$ with α the wave vector outside the barrier. Figure 14 shows G for the four SL types. Notice the clear differences in 1) the onset of the conductance and 2) the number and amplitude of the oscillations.

Bound states. To describe bound states we assume that there are no propagating states, i.e., α and β are imaginary or complex (the latter case can be solved separately), and only the eigenstates with exponentially decaying behaviour are nonzero leading to the relation

$$\begin{pmatrix} f_d \\ 0 \\ e_d \\ 0 \end{pmatrix} = \mathcal{N} \begin{pmatrix} 0 \\ f_g \\ 0 \\ e_g \end{pmatrix}. \tag{3.9}$$

From this relation we can find the dispersion relation for the bound states.

To study the localized states for the anti-symmetric potential profile (Martin *et al.*, 2008; Martinez *et al.*, 2009) we will use a sharp kink profile (step function). The spectrum found by the method above is shown in Fig. 15(a). We see that there are two bound states, both with negative group velocity $v_y \propto \partial\varepsilon/\partial k_y$, as found previously by (Martin *et al.*, 2008). No bound state near zero energy was found for $k_y \to \infty$ in contradiction with (Martinez *et al.*, 2009). For zero energy we find the
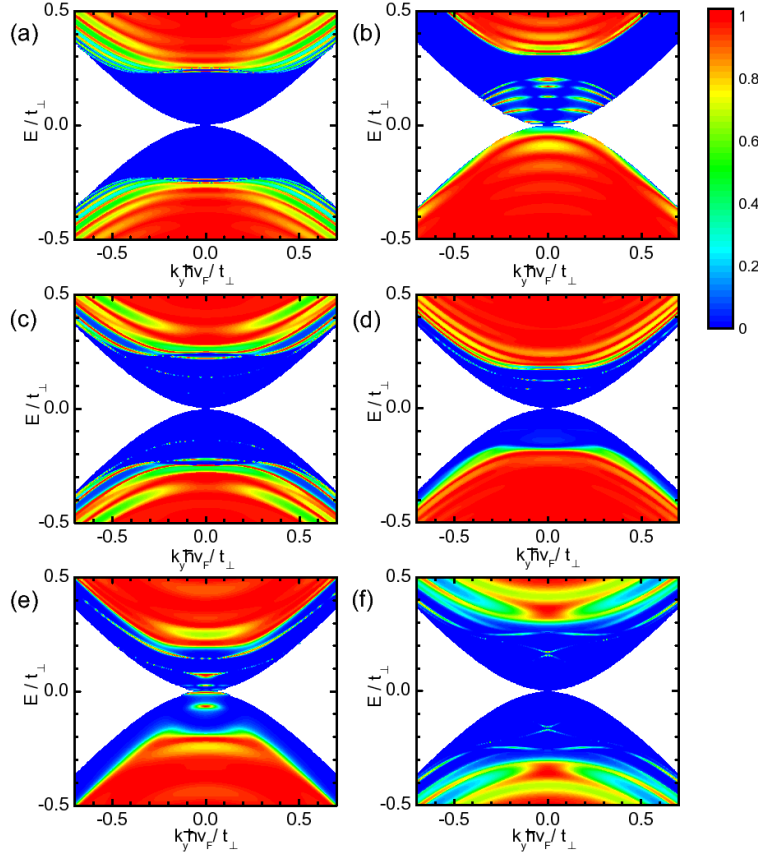
Figure 13. (Color online) Contour plot of the transmission through a single barrier in (a) and (b), for width $W_b = 50$ nm, and through double barriers in (c), (d), (e), and (f) of equal widths $W_b = 20$ nm that are separated by $W_w = 20$ nm. Other parameters are as follows: (a) $\Delta_b = 100$ meV, $V_b = 0$ meV. (b) $\Delta_b = 20$ meV, $V_b = 50$ meV. (c) *Type I*: $V_b = V_w = 0$ meV, $\Delta_w = 20$ meV, and $\Delta_b = 100$ meV. (d) *Type II*: $Vb = -Vw = 20$ meV, $\Delta_w = \Delta = 50$ meV, (e) *Type III*: $V_b = -V_w = 50$ meV, $\Delta_w = \Delta_b = 20$ meV. (f) *Type IV*: $V_b = V_w = 0$ meV, $\Delta_b = -\Delta_w = 100$ meV.

solution

$$k_y = \pm\frac{1}{2}[\Delta^2 + (\Delta^4 + 2\Delta^2 t_\perp^2)^{1/2}]^{1/2}$$
$$\approx \pm\sqrt{\Delta t_\perp}/2^{3/4}, \quad \Delta \ll t_\perp; \tag{3.10}$$

the approximation on the second line leads to the expression found by (Martin *et al.*, 2008).

(*b*) *Superlattices*

The heterostructures above (see Fig. 11), can be used to create four different types of SLs (Dragoman *et al.*, 2010). We will especially focus on type IV and type III SLs in certain limiting cases.
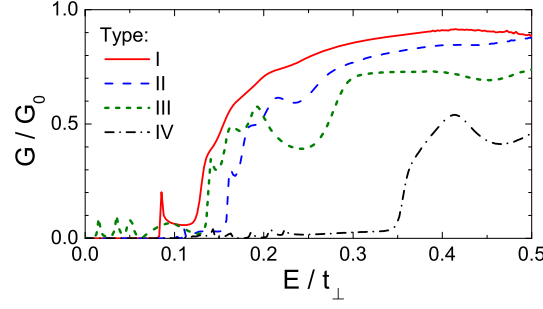
Figure 14. (Color online) Two-terminal conductance of four equally spaced barriers vs energy for $W_b = W_w = 10$ nm and different SL types I-IV. The solid red curve (type I) is for $\Delta_b = 50$ meV, $\Delta_w = 20$ meV, and $V_w = V_b = 0$. The blue dashed curve (type II) is for $\Delta_b = \Delta_w = 50$ meV and $V_b = -V_w = 20$ meV. The green dotted curve (type III) is for $\Delta_b = \Delta_w = 20$ meV and $V_b = -V_w = 50$ meV. The black dash-dotted curve (type IV) is for $\Delta_b = -\Delta_w = 50$ meV and $V_w = V_b = 0$.
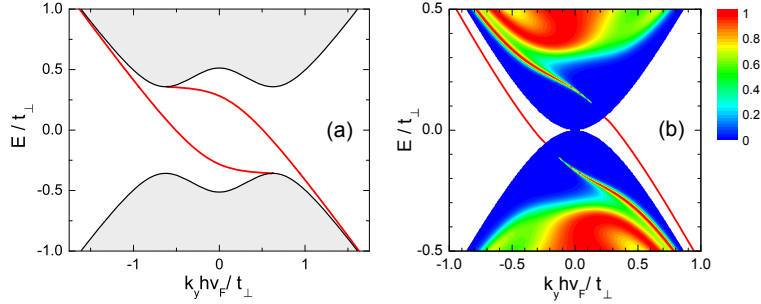

Figure 15. (a) Bound states of the anti-symmetric potential profile (type IV) with bias $\Delta_w = -\Delta_b = 200$ meV. (b) Contour plot of the transmission through a 20 nm wide barrier consisting of two regions with opposite biases $\Delta = \pm 100$ meV.

For a type I SL we see in Fig. 16(a) that the conduction and valence band of the bilayer structure are qualitatively similar to those in the presence of a uniform bias. Type II structures maintain this gap, see Fig. 16(b), as there is a range in energy for which there is a gap in the SL potential in the barrier and well regions. In type III structures we have two interesting features, which can close the gap. First we see from Fig. 12(b) that for zero bias, similar to single-layer graphene, extra Dirac points appear for $k_x = 0$, likewise for Fig. 4(d). In the case $W_b = W_w = L/2 = W$, $k_x = 0$ and $E = 0$ the values for the k_y where extra Dirac points occur are given by the following transcendental equation

$$[\cos(\alpha W)\cos(\beta W) - 1] + \frac{\alpha^2 + \beta^2 - 4ky^2}{2\alpha\beta}\sin(\alpha W)\sin(\beta W) = 0. \qquad (3.11)$$

Comparing the figures 12(b) and 4(d) we remark that, different from the single-layer case, for bilayer graphene the bands in the barrier region are not only flat in the x direction for large k_y values but also for small k_y. The latter corresponds to the zero transmission value inside the barrier region for tunneling through a
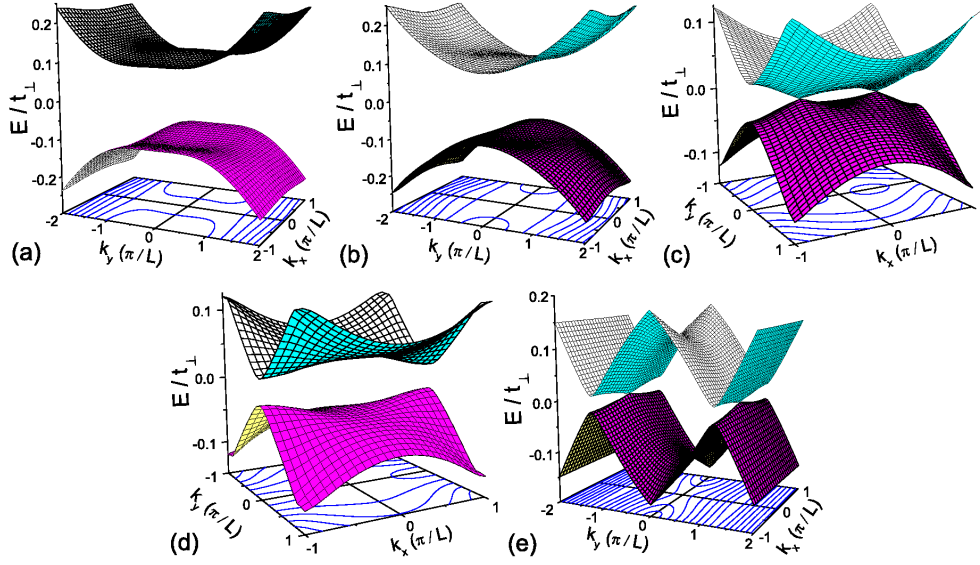
Figure 16. (Color online) Lowest conduction and highest valence band of the spectrum for a square SL with period $L = 20$ nm and $W_b = W_w = 10$ nm. (a) *Type I*: $\Delta_b = 100$ meV and $\Delta_w = 0$. (b) *Type II*: As in (a) for $\Delta_b = \Delta_w = 50$ meV, and $V_b = -V_w = 25$ meV. (c) *Type III*: $V_b = -V_w = 25$ meV, and $\Delta_b = \Delta_w = 0$. (d) *Type III*: $V_b = -V_w = 50$ meV and $\Delta_b = \Delta_w = 0$. (e) *Type IV*: Plot of the spectrum for a square SL with average potential $V_b = V_w = 0$ and $\Delta_b = -\Delta_w = 100$ meV. The contours are for the conduction band and show that the dispersion is almost flat in the x direction.

single unbiased barrier in bilayer graphene. Secondly, if there are no extra Dirac points (small parameter uL) for certain SL parameters, the gap closes at two points at the Fermi-level for $k_y = 0$. The latter we will investigate a bit more in the extended Kronig-Penney model. Periodically changing the sign of the bias (type IV) introduces a splitting of the charge neutrality point along the k_y axis; this agrees with what was found by (Martin *et al.*, 2008). We illustrate that in Fig. 13(e) for a SL with $\Delta_b = -\Delta_w = 100$ meV. We also see that the two valleys in the spectrum are rather flat in the x direction. Upon increasing the parameter ΔL, the two touching points shift to larger $\pm k_y$ and the valleys become flatter in the x direction. For all four types of SLs the spectrum is anisotropic and results in very different velocities along the x and y directions.

Extended Kronig-Penney model. To understand which SL parameters lead to the creation of a gap we look at the Kronig-Penney limit of type III SLs for zero bias (Barbier *et al.* 2010, unpublished work). Also we choose the extended Kronig-Penney model to ensure spectra symmetric with respect to the zero-energy value, such that the zero-energy solutions can be traced down more easily. If the latter zero modes exist, there is no gap. To simplify the calculations we restrict the spectrum to that for $k_y = 0$. This assumption is certainly not valid if the parameter uL is large because in that case we expect extra Dirac points (not in the KP limit) to appear that will close the gap. The spectrum for $k_y = 0$ is determined by the

transcendental equations

$$\cos k_x L = \cos \alpha L \cos^2 P + D_\alpha \sin^2 P, \tag{3.12a}$$

$$\cos k_x L = \cos \beta L \cos^2 P + D_\beta \sin^2 P, \tag{3.12b}$$

with $D_\lambda = \left[(\lambda^2 + \varepsilon^2) \cos \lambda L - \lambda^2 + \varepsilon^2\right]/4\lambda^2 \varepsilon^2$, and $\lambda = \alpha, \beta$. To see whether there is a gap in the spectrum we look for a solution with $\varepsilon = 0$ in the dispersion relations. This gives two values for k_x where zero energy solutions occur

$$k_{x,0} = \pm \arccos[1 - (L^2/8) \sin^2 P]/L, \tag{3.13}$$

and the crossing points are at $(\varepsilon, k_x, k_y) = (0, \pm k_{x,0}, 0)$. If the $k_{x,0}$ value is not real, then there is no solution at zero energy and a gap arises in the spectrum. From Eq. (3.12a) we see that for $\sin^2 P > 16/L^2$ a band gap arises.

Conductivity. In bilayer graphene the diffusive dc conductivity, given by Eq. (2.27), takes the form

$$\sigma_{\mu\mu}(\varepsilon_F)/\sigma_0 = (k_F^3/4\pi\varepsilon_F^2)\left[1 \pm \delta/2(k_F^2 \delta + 1/4)^{1/2}\right]^2, \tag{3.14}$$

with $k_F = [\varepsilon_F^2 + \Delta^2 \mp (\varepsilon_F^2 \delta - \Delta^2)^{1/2}]^{1/2}$, $\delta = 1 + 4\Delta^2$, and $\sigma_0 = e^2 \tau_F t_\perp/\hbar^2$.
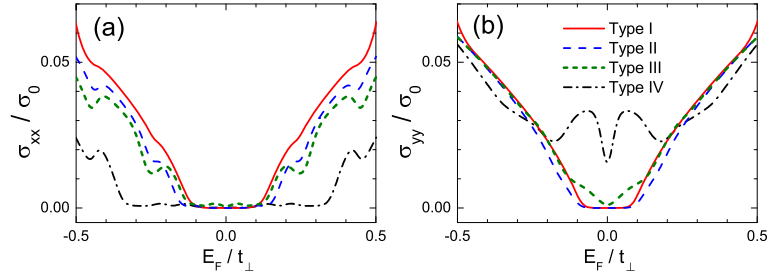

Figure 17. (Color online) Conductivities, σ_{xx} in (a) and σ_{yy} in (b), vs Fermi energy for the four types of SLs with $L = 20$ nm and $W_b = W_w = 10$ nm, at temperature $T = 45K$; $\sigma_0 = e^2 \tau_F t_\perp/\hbar^2$. *Type I*: $\Delta_b = 50$ meV, $\Delta_w = 25$ meV and $V_b = V_w = 0$. *Type II*: $\Delta_b = \Delta_w = 25$ meV and $V_b = -V_w = 50$ meV. *Type III*: $\Delta_b = \Delta_w = 50$ meV and $V_b = -V_w = 25$ meV. *Type IV*: $\Delta_b = -\Delta_w = 100$ meV and $V_b = V_w = 0$.

In Figs. 17(a), (b) the conductivities σ_{xx} in (a) and σ_{yy} in (b) for bilayer graphene are shown for the various types of SLs defined in Sec. 3(b). Notice that for type IV SL the conductivities σ_{xx} and σ_{yy} differ substantially due to the anisotropy in the spectrum.

4. Conclusions

We reviewed the electronic band structure of single-layer and bilayer graphene in the presence of 1D periodic potentials. In addition, we investigated the conditions that lead to carrier collimation in single-layer graphene and determined when extra Dirac points appear in the spectrum and what their influence is on the conductivity. Furthermore, we investigated the tunnelling through, and bound states created by,

simple barrier structures. In single-layer graphene we found that the SL spectrum can be linked to the bound states of a combined barrier and a well.

In bilayer graphene we considered transport through different types of heterostructures, where we distinguished between four types of band alignments. We also connected the bound states in an anti-symmetric potential (type IV) with the transmission through such a potential barrier. Furthermore, we investigated the same four types of band alignments in SLs. The differences between the four types of SLs are reflected not only in the spectrum but also in the conductivities parallel and perpendicular to the SL direction. For type III SLs, which have a zero bias, we found a feature in the spectrum similar to the extra Dirac points found for single-layer graphene. Also, for not too large strengths of the SL barriers we found that the valence and conduction bands touch at points in $\mathbf{k}$ space with $k_y = 0$ and nonzero k_y. Type IV SLs tend to split the K (K') valley into two valleys.

In the Kronig-Penney limit, where we take the barriers to be δ functions $V(x)/\hbar v_F = P\delta(x)$, we saw that the SL spectra, the transmission, conductance, etc., are periodic in the strength of the barriers. As s well known, this is not the case for standard electrons. An important qualitatively new feature is encountered in the extended Kronig-Penney limit for $P = (n + 1/2)\pi$, see Sec. 2(d): the Dirac point becomes a Dirac line.

We expect that these relatively recent findings, that we reviewed in this work, will be tested experimentally in the near future.

References

Abergel, D. S. L., Apalkov, V., Berashevich, J., Ziegler, K. & Chakraborty, T. 2010 Properties of graphene: A theoretical perspective.
Abergel, D. S. L., Apalkov, V., Berashevich, J., Ziegler, K. and Chakraborty, Tapash 2010 Properties of graphene: a theoretical perspective, Advances in Physics, 59: 4, 261 482

Arovas, D. P., Brey, L., Fertig, H. A., Kim, E. & Ziegler, K. 2010 Dirac Spectrum in Piecewise Constant One-Dimensional Potentials. *ArXiv e-prints*.

Barbier, M., Peeters, F. M., Vasilopoulos, P. & Pereira Jr, J. M. 2008 Dirac and klein-gordon particles in one-dimensional periodic potentials. *Phys. Rev. B*, **77**(11), 115 446. (doi:10.1103/PhysRevB.77.115446)

Barbier, M., Vasilopoulos, P. & Peeters, F. M. 2009*a* Dirac electrons in a kronig-penney potential: Dispersion relation and transmission periodic in the strength of the barriers. *Phys. Rev. B*, **80**(20), 205 415. (doi:10.1103/PhysRevB.80.205415)

Barbier, M., Vasilopoulos, P. & Peeters, F. M. 2010 Extra dirac points in the energy spectrum for superlattices on single-layer graphene. *Phys. Rev. B*, **81**(7), 075 438. (doi:10.1103/PhysRevB.81.075438)

Barbier, M., Vasilopoulos, P., Peeters, F. M. & Pereira Jr, J. M. 2009*b* Bilayer graphene with single and multiple electrostatic barriers: Band structure and transmission. *Phys. Rev. B*, **79**(15), 155 402. (doi:10.1103/PhysRevB.79.155402)

Bliokh, Y. P., Freilikher, V., Savel'ev, S. & Nori, F. 2009 Transport and localization in periodic and disordered graphene superlattices. *Phys. Rev. B*, **79**(7), 075 123. (doi:10.1103/PhysRevB.79.075123)

Brey, L. & Fertig, H. A. 2009 Emerging zero modes for graphene in a periodic potential. *Phys. Rev. Lett.*, **103**(4), 046 809. (doi:10.1103/PhysRevLett.103.046809)

Castro, E. V., Novoselov, K. S., Morozov, S. V., Peres, N. M. R., dos Santos, J. M. B. L., Nilsson, J., Guinea, F., Geim, A. K. & Neto, A. H. C. 2007 Biased bilayer graphene: Semiconductor with a gap tunable by the electric field effect. *Phys. Rev. Lett.*, **99**(21), 216 802. (doi:10.1103/PhysRevLett.99.216802)

Castro Neto, A. H., Guinea, F., Peres, N. M. R., Novoselov, K. S. & Geim, A. K. 2009 The electronic properties of graphene. *Rev. Mod. Phys.*, **81**(1), 109–162. (doi:10.1103/RevModPhys.81.109)

Charbonneau, M., van Vliet, K. M. & Vasilopoulos, P. 1982 Linear response theory revisited. III. one-body response formulas and generalized Boltzmann equations. *J. Math. Phys.*, **23**(2), 318–336.

Dragoman, D., Dragoman, M. & Plana, R. 2010 Tunable electrical superlattices in periodically gated bilayer graphene. *J. Appl. Phys.*, **107**(4), 044 312. (doi:10.1063/1.3309408)

Giovannetti, G., Khomyakov, P. A., Brocks, G., Kelly, P. J. & van den Brink, J. 2007 Substrate-induced band gap in graphene on hexagonal boron nitride: Ab initio density functional calculations. *Phys. Rev. B*, **76**(7), 073 103. (doi:10.1103/PhysRevB.76.073103)

Gomes, J. V. & Peres, N. M. R. 2008 Tunneling of dirac electrons through spatial regions of finite mass. *J. Phys.: Condensed Matter*, **20**(32), 325 221.

Ho, J. H., Chiu, Y. H., Tsai, S. J. & Lin, M. F. 2009 Semimetallic graphene in a modulated electric potential. *Phys. Rev. B*, **79**(11), 115 427. (doi:10.1103/PhysRevB.79.115427)

Huard, B., Sulpizio, J. A., Stander, N., Todd, K., Yang, B. & Gordon, D. G. 2007 Transport measurements across a tunable potential barrier in graphene. *Phys. Rev. Lett.*, **98**(23), 236 803. (doi:10.1103/PhysRevLett.98.236803)

Katsnelson, M. I., Novoselov, K. S. & Geim, A. K. 2006 Chiral tunnelling and the klein paradox ingraphene. *Nat. Phys.*, **2**(9), 620–625. (doi:10.1038/nphys384)

Klein, O. 1929 Die reflexion von elektronen an einem potentialsprung nach der relativistischen dynamik von dirac. *Zeitschrift für Physik A Hadrons and Nuclei*, **53**(3), 157–165. (doi:10.1007/BF01339716)

Martin, I., Blanter, Y. M. & Morpurgo, A. F. 2008 Topological confinement in bilayer graphene. *Phys. Rev. Lett.*, **100**(3), 036 804. (doi:10.1103/PhysRevLett.100.036804)

Martinez, J. C., Jalil, M. B. A. & Tan, S. G. 2009 Robust localized modes in bilayer graphene induced by an antisymmetric kink potential. *Appl. Phys. Lett.*, **95**(21), 213106. (doi:10.1063/1.3263150)

McCann, E. 2006 Asymmetry gap in the electronic band structure of bilayer graphene. *Phys. Rev. B*, **74**(16), 161 403. (doi:10.1103/PhysRevB.74.161403)

Novoselov, K. S., Geim, A. K., Morozov, S. V., Jiang, D., Zhang, Y., Dubonos, S. V., Grigorieva, I. V. & Firsov, A. A. 2004 Electric field effect in atomically thin carbon films. *Science*, **306**(5696), 666–669. (doi:10.1126/science.1102896)

Park, C.-H., Son, Y.-W., Yang, L., Cohen, M. L. & Louie, S. G. 2009*a* Electron beam supercollimation in graphene superlattices. *Nano Lett.*, **8**(9), 2920–2924. (doi:10.1021/nl801752r)

Park, C.-H., Son, Y.-W., Yang, L., Cohen, M. L. & Louie, S. G. 2009*b* Landau levels and quantum hall effect in graphene superlattices. *Phys. Rev. Lett.*, **103**(4), 046 808. (doi:10.1103/PhysRevLett.103.046808)

Park, C.-H., Yang, L., Son, Y.-W., Cohen, M. L. & Louie, S. G. 2008*a* Anisotropic behaviours of massless dirac fermions in graphene under periodic potentials. *Nat. Phys.*, **4**(3), 213–217.

Park, C.-H., Yang, L., Son, Y.-W., Cohen, M. L. & Louie, S. G. 2008*b* New generation of massless dirac fermions in graphene under external periodic potentials. *Phys. Rev. Lett.*, **101**(12), 126 804. (doi:10.1103/PhysRevLett.101.126804)

Pereira Jr, J. M., Mlinar, V., Peeters, F. M. & Vasilopoulos, P. 2006 Confined states and direction-dependent transmission in graphene quantum wells. *Phys. Rev. B*, **74**(4), 045 424. (doi:10.1103/PhysRevB.74.045424)

Pereira Jr, J. M., Peeters, F. M., Chaves, A. & Farias, G. A. 2010 Klein tunneling in single and multiple barriers in graphene. *Semiconductor Science and Technology*, **25**(3), 033 002. (doi:10.1088/0268-1242/25/3/033002)

Pereira Jr, J. M., Vasilopoulos, P. & Peeters, F. M. 2007*a* Graphene-based resonant-tunneling structures. *Appl. Phys. Lett.*, **90**(13), 132122. (doi:10.1063/1.2717092)

Pereira Jr, J. M., Vasilopoulos, P. & Peeters, F. M. 2007*b* Tunable quantum dots in bilayer graphene. *Nano Lett.*, **7**(4), 946–949. (doi:10.1021/nl062967s)

Roslyak, O., Iurov, A., Gumbs, G. & Huang, D. 2010 Unimpeded tunneling in graphene nanoribbons. *J. Phys.: Condensed Matter*, **22**(16), 165 301.

San-Jose, P., Prada, E., McCann, E. & Schomerus, H. 2009 Pseudospin valve in bilayer graphene: Towards graphene-based pseudospintronics. *Phys. Rev. Lett.*, **102**(24), 247 204. (doi:10.1103/PhysRevLett.102.247204)

Schliemann, J., Loss, D. & Westervelt, R. M. 2005 Zitterbewegung of electronic wave packets in iii-v zinc-blende semiconductor quantum wells. *Phys. Rev. Lett.*, **94**(20), 206 801. (doi:10.1103/PhysRevLett.94.206801)

Sun, J., Fertig, H. A. & Brey, L. 2010 Effective Magnetic Fields in Graphene Superlattices. *ArXiv e-prints.*

Wang, L.-G. & Zhu, S.-Y. 2010 Electronic band gaps and transport properties in
graphene superlattices with one-dimensional periodic potentials of square barriers. *Phys. Rev. B*, **81**(20), 205 444. (doi:10.1103/PhysRevB.81.205444)

Winkler, R., Zülicke, U. & Bolte, J. 2007 Oscillatory multiband dynamics of free
particles: The ubiquity of zitterbewegung effects. *Phys. Rev. B*, **75**(20), 205 314.
(doi:10.1103/PhysRevB.75.205314)

Young, A. F. & Kim, P. 2009 Quantum interference and klein tunnelling in
graphene heterojunctions. *Nat. Phys.*, **5**(3), 222–226. (doi:10.1103/PhysRevLett.
98.236803)

Zawadzki, W. 2005 Zitterbewegung and its effects on electrons in semiconductors.
Phys. Rev. B, **72**(8), 085 217. (doi:10.1103/PhysRevB.72.085217)